Strain analysis by inversion of coherent Bragg X-ray diffraction intensity: the illumination problem

Virginie Chamard, Mickaël Dollé, G. Baldinozzi, F. Livet, M. de Boissieu, S. Labat, F. Picca, C. Mocuta, P. Donnadieu, T.H. Metzger

Strain analysis by inversion of coherent Bragg X-ray diffraction intensity: the illumination problem

V. Chamard[a]*, M. Dollé[b], G. Baldinozzi[c], F. Livet[d], M. de Boissieu[d], S. Labat[a], F. Picca[e], C. Mocuta[e], P. Donnadieu[d] and T.H. Metzger[f]

[a]*IM2NP, CNRS, Université Aix-Marseille, 13397 Marseille Cedex 20, France;* [b]*CEMES-CNRS, BP 94347, 31055 Toulouse Cedex, France;* [c]*SPMS-Ecole Centrale Paris, 92295 Chatenay-Malabry, France;* [d]*SIMaP, 38402 Saint-Martin d'Héres Cedex, France;* [e]*Synchrotron Soleil, L'Orme des Merisiers Saint-Aubin, 91192 Gif-sur-Yvette, France;* [f]*ESRF, BP 220, 38043 Grenoble Cedex, France*

Bragg coherent X-ray diffraction imaging is demonstrated with a micro-focused illumination. The 2D projected density of the 3D nano-crystal is successfully retrieved from the inversion of its diffraction intensity pattern. The analysis of the phase field at the sample position, which holds in principle the strain information, emphasizes the high sensitivity of the technique with regard to the wavefront structure. The ptychography approach is a proposed solution to discriminate the wavefront function from the sample electron density distribution. It is based on a redundancy of the collected information obtained by measuring a series of diffraction patterns for different but overlapping beam positions onto the sample. Applicability to the Bragg geometry still needs to be demonstrated.

Keywords: inversion problem; coherent X-ray diffraction; strain analysis; nano-crystals; nano-focusing

1. Introduction

Hard X-rays – with a wavelength in the nm range – are the most appropriate waves to reveal new insight in material science [1,2]. Recently, with the development of brilliant X-ray sources such as second- and third-generation synchrotrons, the X-ray study of nano-structured materials has become possible [3–5]. The weak interaction of the X-ray photons with matter allows for a non-destructive investigation of the nano-structure directly in its environment (embedded in a matrix, during growth, under stress, etc.). But, the impossibility of measuring the phase of the diffracted field, also known as the 'phase problem', is a strong limitation to the method. Therefore, analysis of the diffraction patterns are often model-dependent [3].

In the 1950s, it was, however, demonstrated that retrieving the phase directly from the intensity information is possible if the diffraction pattern is sampled at a frequency slightly larger than twice the Nyquist frequency of the scattered wavefield [6]. It corresponds to confining the direct space object to a finite region called the support, which occupies half of the total volume given by the computational window. Outside the support, the space is filled with zeros. As this problem has no analytical solution, the inversion relies on numerical iterative algorithms using back and forth transforms between the sample and the measurement spaces [7,8]. This lens-less microscopy technique, also known as coherent X-ray diffraction imaging (CDI) requires a coherent illumination of the sample. (Partially) coherent X-ray beams are nowadays provided by highly brilliant third-generation synchrotron sources such as, e.g. the ESRF or Soleil in France, SLS in Switzerland, APS in the US, Spring8 in Japan, and so on.

The first demonstration of CDI was obtained in 1999 by Miao and his co-workers for two-dimensional non-crystalline test objects [9], followed rapidly by the 3D demonstration [10]. Another important step is achieved by Robinson and his co-workers. They demonstrate the imaging of a nano-crystal in 2D [11] and in 3D [12], from the inversion of intensity patterns measured in Bragg geometry. The periodic atomic structure of the crystal leads to additional reciprocal space maxima called the Bragg peaks. When the whole sample is coherently illuminated, each Bragg diffraction peak presents a finely structured intensity distribution related to the crystal shape and electron density. With planar wavefield illumination and far-field detection, the scattering process is described in a good approximation by the Fourier transform of an effective complex-valued electron density $g(\mathbf{r}) = \rho(\mathbf{r})\exp(i\phi(\mathbf{r}))$, where $\rho(\mathbf{r})$ is the electron density of the unstrained

*Corresponding author. Email: virginie.chamard@univ-cezanne.fr

crystal and $\phi(\mathbf{r})$ is the phase given by the crystal displacement field $\mathbf{u}(\mathbf{r})$ projected onto the Bragg vector $\mathbf{G}$ [13,14]. Hence, similar iterative algorithms can be used in CDI and Bragg CDI for the inversion of the intensity diffraction pattern. While CDI is encountering a fast development with recent results in the imaging of complex noncrystalline media such as ceramic nanofoam [15] and biological samples [16,17], strain imaging using Bragg CDI remains more difficult to address. Recently, the 3D reconstruction of the displacement field in a Pb nanocrystal has been presented [18]. Thanks to the large angles necessary to reach the Bragg reflections, Bragg geometry presents the advantage, in contrast to CDI, of avoiding the contribution of the direct beam illumination. However, several aspects have to be carefully considered in order to successfully retrieve the exit wavefield at the sample in Bragg CDI. The weakness of the Bragg intensity scattered by a nano-crystal is a first strong limitation and it requires, at least, a long acquisition time and therefore a highly stable experimental set-up [19,20]. In addition, the complex-valued density function requires an adaptation of the iterative algorithm: in particular, for highly strained crystals, the nonlinear behavior of the non-homogeneous displacement field leads to an intensity distribution that can become very different from the Fourier transform of the crystal shape function. This behavior leads to serious convergence problems. In that case, one has to seek for additional direct space constraints, specific to the studied system, in order to reach the convergence [21–23]. For weakly strained systems, the phase of the retrieved complex-valued electron density often presents some variations that are related to the experimental conditions rather than to the crystal structure [19,24]. In a previous paper, we investigated the detection related artifacts [24]. In this work, we describe the influences of other artifacts, such as reciprocal space offset, refraction effects and curved illumination wavefront.

The paper is organized as follows: the sample and the experimental set-up used for Bragg CDI with a micro-focused beam are described in Section 2 before the inversion schemes and results are presented in Section 3. In Section 4, the retrieved quantity is compared to calculations taking into account experimental artifacts such as the illumination wavefront curvature. Finally, in Section 5, the actual limits of the technique are discussed, as well as its perspectives for strain analysis at the nanometer scale.

2. Experiment

The sample used for this experiment is a nano-sized crystalline powder (a non-stoichiometric $ZrC_{0.92}O_{0.03}$ compound), prepared by a sol-gel technique. Further details concerning the sample preparation can be found in [25]. The powder is composed of well-defined single-crystals with mostly often octahedron-like shape (Figure 1(*a*)). No strong displacement field (due to strain or crystal defects) is revealed by transmission electron microscopy (TEM) measurements (Figure 1(*b*)). The particle typical size is in the 100–300 nm range.

The CDI experiment was carried out at the ID01 beamline (ESRF, France). The monochromatic 9.5 keV beam (wavelength $\lambda = 0.13$ nm) was delivered by a double crystal Si(111) monochromator (bandwidth of about 10^{-4}, resulting in a longitudinal

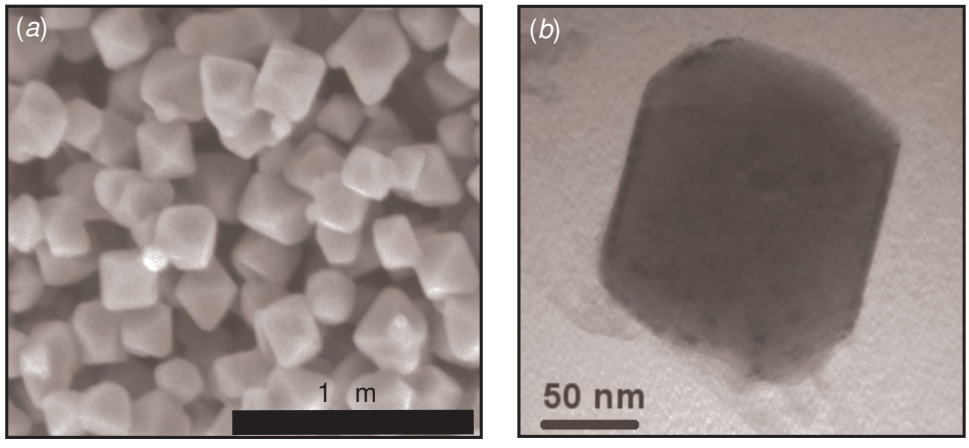

Figure 1. (*a*) Scanning electron microscopy picture of the ZrCO nano-powder. (*b*) Transmission electron microscopy picture of a single ZrCO nano-crystal.

(temporal) coherence length of 0.5 μm). The experimental set-up is shown in Figure 2(*a*). The beam defining slits (S1) located at about 36 m from the source and 10 m from the sample were closed down to 300 μm. With this setting, the transverse coherence length was estimated to about 5 μm. However, due to the monochromator instabilities (cooling system) and the use of two focusing mirrors (higher harmonics rejection), which act as non-perfect optical elements, the transverse coherence length was certainly smaller [26]. The small size of the sample, in the nm range, required the use of a focusing optics in order to increase the coherent flux at the sample position [27]. Therefore, a set of 46 Be compound refractive lenses (CRLs), located 0.9 m upstream the sample, was introduced to further focus the beam to a $4 \times 8\,\mu m^2$ (horizontal × vertical, FWHM) spot at the sample position, with an integrated intensity of 2×10^9 photons/s. Contrarily to Fresnel zone plate focusing optics, which create a planar wavefront at the focus when used in the diffraction limited condition [28,29], ideal CRLs would transform the perfect incoming planar illumination into a spherical wavefront. However, as both illumination function and Be CRLs are non-perfect, it is expected that the wavefront at the focus is highly complex. In order to maximize the intensity-to-noise ratio, the entrance slits (S2) of the focusing optics were symmetrically opened to 200 μm, much larger than the transverse coherence length. An estimate of the experimental coherence condition can be given from the product of the source size σ by the beam divergence ϵ: appropriate coherence conditions are obtained when $\sigma\epsilon \leq \lambda$ is fulfilled [30]. For this set-up, the partially coherent beam exhibited a maximum geometrical beam divergence ε of about 0.03 mrad. Due to the sample finite size together with the Bragg geometry, the beam size was estimated to about 100 nm at the sample position (only the part of the beam illuminating the isolated crystal is scattered). The left-hand term of the relation gives about 3×10^{-12} m, showing that the coherence conditions were completely fulfilled. This was further confirmed by the observation of strongly visible interference fringes in the diffraction pattern. The intensity acquisition was performed with a direct illumination charge coupled device (CCD) camera from Princeton (384×576 pixels of $22.5 \times 22.5\,\mu m^2$ size each) mounted at 30 cm from the sample. The ZrC powder was deposited onto a SiO_2/Si substrate (with a surface density of a few particles/μm^2) previously covered by a conductive C thin film in order

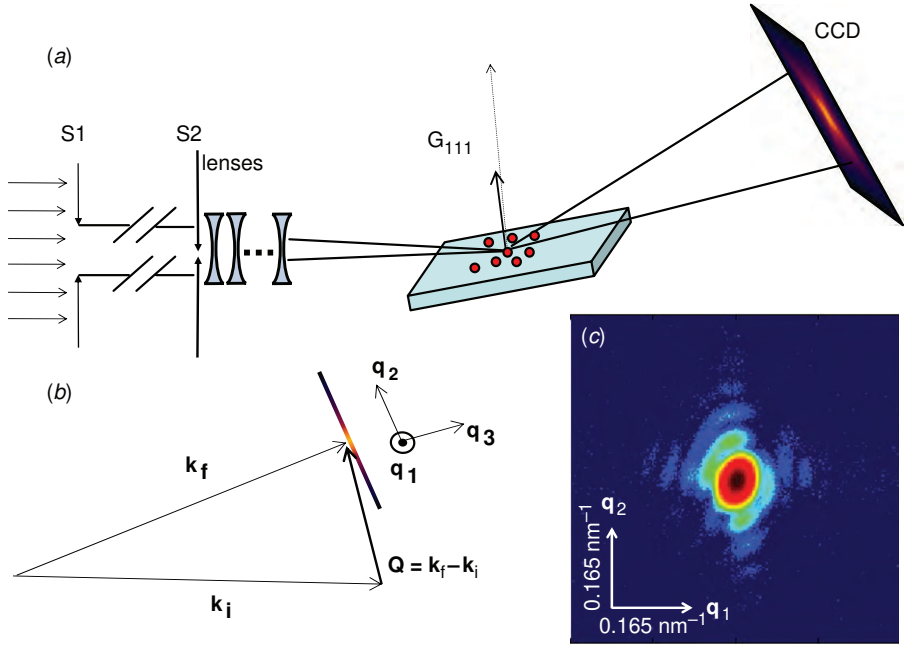

Figure 2. (*a*) Experimental set-up used at the ID01 beamline (ESRF) for the coherent X-ray diffraction experiment with a micro-focused beam. (*b*) Experimental geometry. (*c*) Coherent X-ray diffraction pattern measured at the ZrC 111 reflection on a single nano-crystal. (The color version of this figure is included in the online version of the journal.)

to evacuate the electrostatic charges and the heat load induced by the focused X-ray beam, allowing thereby the stability of the sample.

In Bragg CDI, the coherently scattered intensity is measured as a function of the wavevector transfer $\mathbf{Q}$, which is given by $\mathbf{Q}=\mathbf{k}_f-\mathbf{k}_i$, where $\mathbf{k}_i$ (respectively $\mathbf{k}_f$) is the incident (respectively diffracted) wavevector (with $k_{i,f}=2\pi/\lambda$). The 2D coherent diffraction pattern is obtained after carefully aligning the wavevector transfer $\mathbf{Q}$ defined by the center of the CCD with regard to the 111 Bragg reflection ($\mathbf{G}_{111}$) of the crystal. Therefore, the wavevector transfer $\mathbf{Q}$ can be written as $\mathbf{Q}=\mathbf{G}_{111}+\mathbf{q}$, where the components 1 and 2 of $\mathbf{q}$, (noted q_1, q_2) are taken in the CCD plane, horizontally and vertically, respectively, while the q_3 direction is perpendicular to $\mathbf{G}_{111}$ (Figure 2(*b*)). The center of the 199×199 pixel area shown in Figure 2(*c*) corresponds to $G_{111}=23.2\,\mathrm{nm}^{-1}$, where $q_{1,2,3}=0$. The detector to sample distance and the 111 Bragg angle ($\theta_B=13.88^\circ$) give a pixel resolution $\delta q_{1,2}$ of $3.4\times10^{-3}\,\mathrm{nm}^{-1}$. The uncertainty on q_3 is evaluated to $\delta q_3=4\times1^{0-3}\,\mathrm{nm}^{-1}$, given by the uncertainty of the Bragg peak maximum on the rocking curve. The diffraction pattern shown in Figure 2(*c*) results from the accumulation of 1700 frames with a 2 s exposure time. Each frame is analyzed by the droplet algorithm to recover the single photon signal [31]. The intensity exhibits a dynamic range of a few 10^3. The interference fringes result from the crystal finite size effects, i.e. the facets along the [111] and [$\bar{1}$11] (or the symmetric [1$\bar{1}$1]) directions. The typical angle of about $71^\circ\pm2^\circ$ is measured between the two streaks. The oversampling ratio is more than 10 pixels per interference fringe.

3. Inversion

The principle of the phase retrieval algorithm is shown in Figure 3. The inversion algorithm is initiated with a sample estimate, whose shape fulfills the support condition together with a set of random phases. The nano-crystal sample is small enough to fulfill the Born approximation. The illumination is assumed to be planar and the sample detector distance is large enough to consider the far-field regime is reached. Therefore, the scattered wavefield $G(\mathbf{q})$ can simply be described by the Fourier transform of the sample electron density $g(\mathbf{r})$, which is introduced as a fast Fourier transform (FFT) in the iterative algorithm. In order to allow for the convergence of the algorithm, a set of constraints has to be applied, at each iteration, in the sample and Fourier spaces. One common sample constraint is the support condition of the sample density, which is a direct consequence of the oversampling condition. Another very powerful constraint to reach the convergence is the positivity of the electron density, which is usually used for strain-free material (amorphous system or fully relaxed crystals). However, it cannot be applied in the present case of a

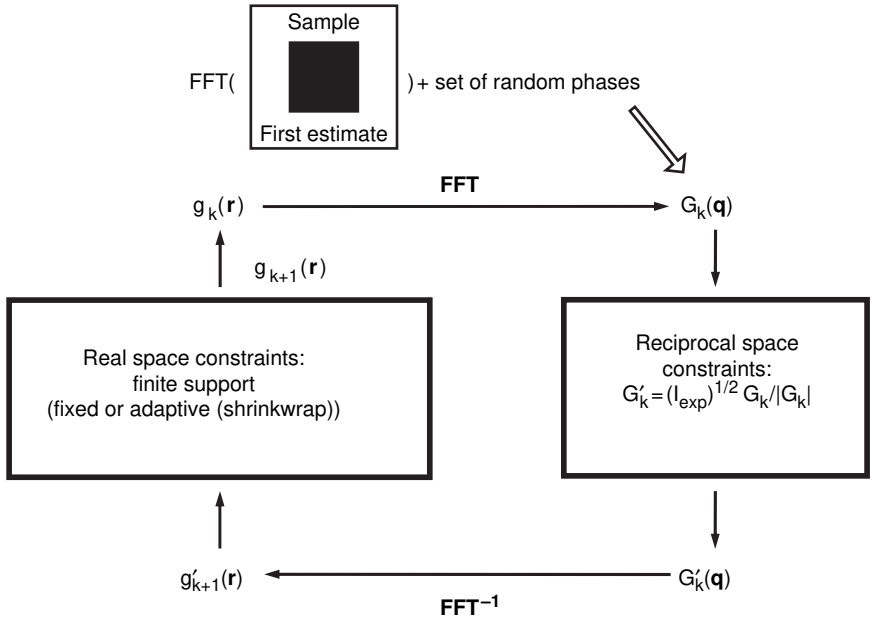

Figure 3. Scheme of the inversion algorithm: $g(\mathbf{r})$ is the sample electron density function and $G(\mathbf{q})$ is the diffracted wavefield at the detector position. For a planar illumination, when Born conditions are fulfilled and the detection is performed in the far-field regime, $G(\mathbf{q})$ is the Fourier transform of $g(\mathbf{r})$. Fast Fourier transforms (FFTs) are used to propagate back and forth the wavefield from the sample to detector positions. The subscripts k and $k+1$ are the iteration indices.

complex-valued electron density. In the Fourier space, the found solution has to fulfill the experimental measurement: the magnitude $|G(\mathbf{q})|$ of the far-field complex-valued scattered wavefield $G(\mathbf{q}) = |G(\mathbf{q})|\exp(i\varphi(\mathbf{q}))$ has to be equal to the square root of the measured intensity $I(\mathbf{q})$. The convergence of the algorithm is reached when the solution fulfills both the sample and the Fourier space constraints. It can be monitored at each iteration by the error metric ξ^2 which is given by:

$$\xi^2 = \frac{\sum_{i=1}^{N} \left(|G_i| - \sqrt{I_i} \right)^2}{\sum_{i=1}^{N} I_i} \quad (1)$$

where the subscript i denotes the pixel number and N the total number of pixels. As the error metric decreases at each iteration, this algorithm is named error reduction (ER) [8]. It is a derivative of the original Gerchberg and Saxton algorithm [7]. However, the convergence of the ER algorithm is rather slow and has to be used alternately with the hybrid input output algorithm (HIO) [8]. The HIO algorithm provides an element of feedback by linearly including a portion of the object solution, obtained by applying the Fourier space constraint, in the solution resulting from the previous iteration, in order to build the solution at the next iteration. Therefore, the real space constraint never enforces the density to be strictly equal to zero outside the support. When it converges, the error metric value is equal to zero. However, for experimental data with noise and limited dynamical range, a zero-error metric cannot be obtained and the algorithm is stopped after ξ^2 becomes smaller than a certain threshold. The obtained solution is approved when different starting guesses (i.e. different sets of initial random phases) lead to similar – almost identical – solutions for the same ER + HIO cycle combination. Our inversion procedure has first been successfully checked on several numerical complex-valued examples [14,32].

For the measurement presented here, the inversion procedure was composed of 15 cycles, each of them being a combination of ER (20 steps) and HIO (50 steps) algorithms. For both algorithms, a complex-valued electron density solution was allowed. After each cycle, the support was re-evaluated to a tighter one using either the shrink wrap method [33] or manual adjustments. Figure 4 presents the magnitude (*a*) and the phase (*b*) of the best reconstruction of the sample electron density. The error metric is smaller than 2×10^{-4}. The extent of the detectable intensity in the Fourier space gives an estimate of the resolution of about $13 \times 13\,\mathrm{nm}^2$.

4. Analysis of the retrieved quantity

The result obtained in Figure 4 demonstrates the possibility to invert the complex valued wavefield from an intensity measurement obtained with a micro-focused illumination. However, in order to quantify the quality of the result, a detailed analysis of the retrieved quantity at the sample plane is presented in the following, for, respectively, the sample magnitude and phase successively.

In a 2D measurement, such as the one presented here, the retrieved quantity at the sample plane is the projection of the 3D complex-valued electron density, onto the detector (2D) plane [14]. In order to illustrate this property, a nano-crystal model, with an octahedron shape is used, as suggested by the SEM observations (Figure 1(*a*)). According to the two streak orientations observed in Figure 2(*c*), one can orientate the octahedron with respect to the CCD plane, with two pairs of facets perpendicular to the diagonal streak and two other facets slightly inclined with regard to the horizontal plane in order to take into account the 111 Bragg angle (Figure 4(*c*)). The density projection onto the CCD plane is further calculated and compared to the retrieved magnitude. The contour of the octahedron projection is plotted as a white dashed line in Figure 4(*a*), while the complete 2D density distribution (not shown here) is comparable to the maps of Figures 5(*a*) and 6(*b*). The quantitative agreement between the experimentally retrieved magnitude and the octahedron model is rather good except that the weak densities in the top right and bottom left corners cannot be retrieved: it is most likely due to the sensitivity of the experiment, limited by the intensity dynamic range. However, a crystal with amorphous corners would give the same discrepancies.

The analysis of the retrieved phase field is more puzzling: it presents a peculiar behavior with a phase value $\phi(\mathbf{r})$ decreasing near the particle edges and an almost radial behavior ($\phi(\mathbf{r}) \approx \phi(r)$). This is clearly different from the constant phase field expected for strain free crystals (no displacement). In order to understand the origin of this phase field, five hypothesis have been tested. They are described in the following.

(i) According to the crystal shape and symmetry, any physically reasonable internal strain field (strain at the surface, at the corners, in the center, etc.) should correspond to an anti-centrosymmetric displacement field. Therefore, the expected phase field $\phi_S(\mathbf{r})$ should exhibit the same anti-centrosymmetric aspect $\phi_S(\mathbf{r}) = -\phi_S(-\mathbf{r})$. The 2D projection of the 3D strained crystal cannot further

transform the symmetry of the 2D retrieved phase field [14]. A centro-symmetric behavior, as the observed one, is very unlikely as long as the displacement field is related to the symmetry of the nano-crystal. Unfortunately, the TEM method, which presents in principle the desired sensitivity towards the displacement field of an atomic array, cannot answer

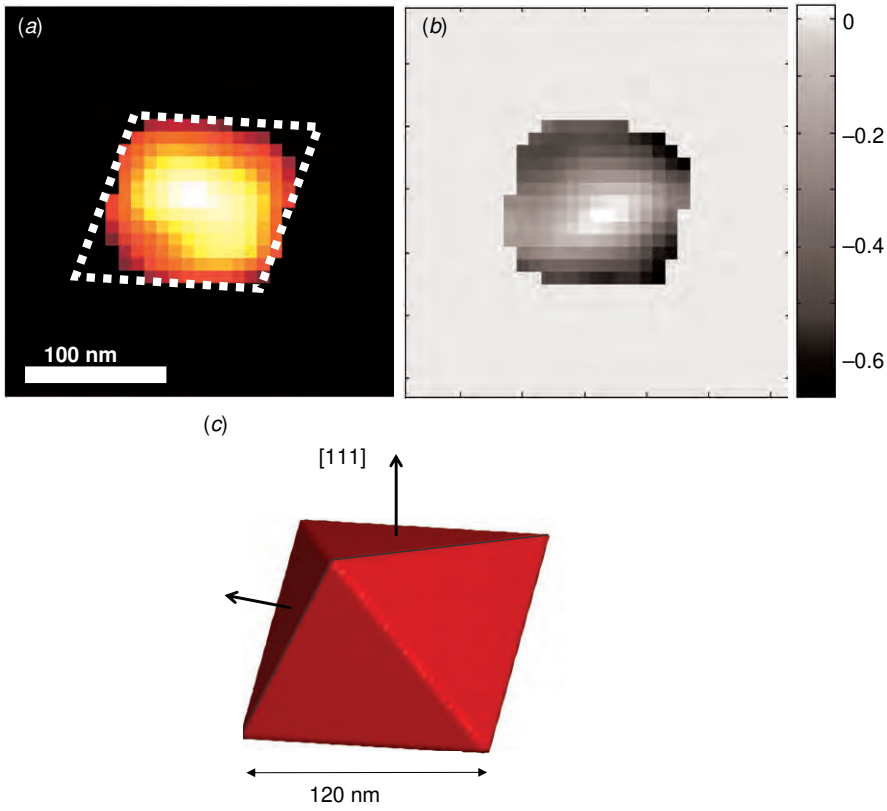

Figure 4. (*a*) Retrieved magnitude, and (*b*) phase of the field at the object plane, resulting from the best inversion result. (*c*) 3D view of an octahedron, as seen from the 2D detector. (The color version of this figure is included in the online version of the journal.)

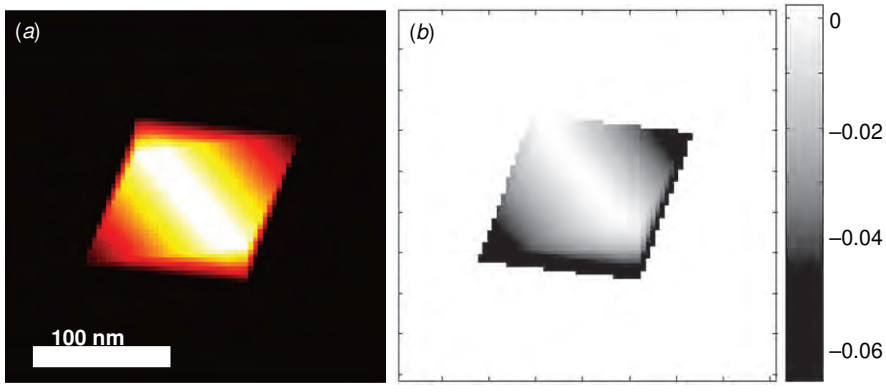

Figure 5. 2D projection of the magnitude (*a*) and phase (*b*) of the wavefield at the sample position calculated for a strain free ZrC octahedron including refraction effects ($\delta = 1.3 \times 10^{-5}$). (The color version of this figure is included in the online version of the journal.)

this question for this sample because TEM requires a constant thickness or displacement along the zone axis. Furthermore, the same sensitivity as the one obtained with the X-ray reconstruction would be very difficult to achieve with TEM for such a nano-particle.

(ii) The crystal is assumed to present a core-shell chemical structure (ZrC + ZrCO): the obtained phase shift $\phi_{CS}(\mathbf{r})$ between the center and the borders of the 2D crystal projection presents the correct centro-symmetric aspect with almost radial dependency, but the phase shift amplitude is found to be in the 10^{-3} rad range, much smaller than the one observed.

(iii) The 2D coherent diffraction pattern is assumed to be slightly off-centered with regard to the Bragg peak maximum (i.e the 2D slice is taken at $q_3 \neq 0$). A straightforward analytical calculation shows that the expected phase $\phi_{OB}(\mathbf{r})$ of the retrieved complex-valued electron density function behaves like $\phi_{OB}(\mathbf{r}) = -\phi_{OB}(-\mathbf{r})$.

(iv) Although the real part of the index of refraction, $1-\delta$, is close to unity, refraction effects may become non-negligible in the crystal because the wave propagation distance is much larger than the wavelength λ. Hence, the wavefield propagating into the crystal is experiencing a phase shift with regard to the wavefield propagating in the absence of matter, both for the incoming and scattered waves. At each position $\mathbf{r}$ in the crystal, the refraction-induced phase shift is given by $\phi_R(\mathbf{r}) = \frac{2\pi}{\lambda}\delta d(\mathbf{r})$, where $d(\mathbf{r})$ is the optical path length difference between the position $\boldsymbol{r}$ and a reference (taken at the upper surface of the ZrC crystal). Hence, the exit wavefield of the 3D crystal is no longer proportional only to the electron density, but exhibits an additional refraction-induced phase shift. This modification is shown in the calculation of the quantity retrieved in our CDI experiment: the exit wavefield is obtained for a 3D ZrC crystal ($\delta = 1.3 \times 10^{-5}$) in the 111 Bragg reflection geometry. In order to compare with the experimental results, the 3D refraction modified exit wavefield is further projected onto a 2D plane parallel to the CCD plane [14]. The 2D amplitude and phase are shown in Figures 5(*a*) and (*b*). While the retrieved amplitude is almost not affected by the refraction effects, the associated phase map is not constant anymore: the phase difference between the center and the sides of the retrieved quantity is in the 0.06 rad range, an order of magnitude smaller than the phase shift difference observed in the experiment (Figure 4(*b*)).

(v) Finally, we consider the effect of a curved wavefront illumination. In this approach, the spherical wavefront is supposed to present a constant radius of curvature R and a constant amplitude over the crystal dimension. The exit wavefield $E_i(\mathbf{r})$ at position $\mathbf{r}$ in the crystal is expressed by

$$E_i(\mathbf{r}) \propto g(\mathbf{r}) \exp(i\mathbf{qr}) \exp(i\phi_C(\mathbf{r})) \qquad (2)$$

where $\phi_C(\mathbf{r})$ is the wavefront-curvature induced phase shift. As seen in Figure 6(*a*), $\phi_C(\mathbf{r}) = \frac{2\pi}{\lambda} l(\mathbf{r})$, where $l(\mathbf{r})$ is the distance, along the propagation direction k_i, between the curved wavefront and a reference planar wavefront. Therefore, the Fourier relation between the far-field scattered wavefield and

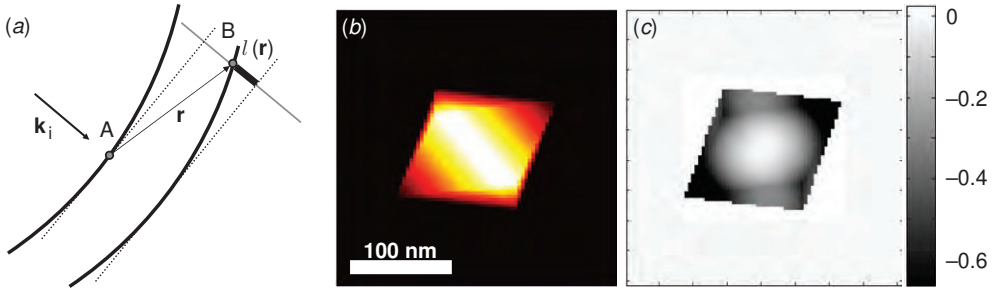

Figure 6. (*a*) Origin of the phase shift $\phi_C(\mathbf{r})$ between A and B, when the illumination beam presents a curved wavefront: $\phi_C(\mathbf{r}) = \frac{2\pi}{\lambda} l(\mathbf{r})$ with $l(\mathbf{r})$ the distance between the curved wavefront in B and the planar wavefront reference taken in A. (*b*) 2D projection of the magnitude and (*c*) phase of the wavefield at the sample position calculated for a spherical illumination wavefront impinging on a strain free ZrC octahedron, such as the one of Figure 4(*c*). (The color version of this figure is included in the online version of the journal.)

a refraction modified electron density is still valid. The 2D retrieved quantities shown in Figures 6(*b*) and (*c*) are calculated, as in the previous case, from the 2D projection of the 3D strain free ZrC crystal onto the detection plane. The result, which is obtained with a curvature radius $R = 90\,\mu m$ agrees very well with the experimental reconstruction: the phase field exhibits the experimentally expected radial symmetry and phase shift amplitude, while the magnitude itself does not exhibit significant modification. It is clear that this calculation is not a definitive proof that the experimentally retrieved phase field is directly resulting from wavefront curvature effects. However, it shows the sensibility of the methods with respect to the finest structures of the X-ray beam. For a CRL focusing set-up, assuming the optical system is perfect, the wavefront at the focal plane is expected to condense into a point-like source that will further propagate as a spherical wave. Therefore, *R* also represents the distance to the focal plane. Ensuring that the nano-crystal is in the focal plane of the CRLs requires a fine monitoring of the distance between the sample and the focus with an accuracy much smaller than 100 μm, which remains challenging regarding the available stability at the existing coherence micro-diffraction beamlines. This could be accomplished through a detailed scanning of the beam size along its propagation direction, using the nano-crystal in diffraction conditions, as a probe. The position of the beam size minimum would then correspond to the focal point. This 100 μm accuracy can be relaxed for larger depth of focus optics. With the focusing set-up presented here, the typical strain limit, below which the method becomes unsensitive, is estimated to about 10^{-3}. Other effects like aberration problems are not introduced here. They would certainly lead to phase artifacts as well.

5. The wavefront problem

Although the high brilliance of third generation synchrotron sources opens the way to coherent X-ray diffraction experiments, the investigation of nano-crystals with typical size in the range of 100 nm requires a further focusing of the beam. In principle, introducing perfect focusing optics on the beam path should not modify the coherence properties of the beam. In a real experiment, X-ray optics cannot be considered as perfect and their introductions slightly affect the coherence properties. However, this modification of the coherence is minimum with regard to the modification of the wavefront profile, which is described by a complex-valued function $P(\mathbf{r})$. The magnitude of the illumination is usually described by a Gaussian profile, while the phase may result in various behaviors, depending on the nature of the focusing elements [28,29]. In that context, the scattered wavefield in the far-field regime is the Fourier transform of the exit wavefield given by the product $P(\mathbf{r}) \times \rho(\mathbf{r})$. Therefore, the retrieved phase at the sample plane is a mixing of the illumination wavefront phase with the effective phase of the sample density itself. The presented result is an illustration of this problem. In the recent past, other groups have also observed similar effects [12,27,34] and strategies are now developed to finely characterize the wavefront illumination function [35,36]. We describe in the following the ptychography approach as a possible solution for the wavefield illumination problem.

Contrarily to CDI, where the convergence of the algorithm is ensured by the oversampling condition, the ptychography approach developed by Rodenburg and his co-workers [37] is based on the partial redundancy of the collected information: the beam is scanned onto the sample and the coherently scattered intensity patterns are collected for each beam position, ensuring that the different beam positions verify a partial but strong overlapping of their footprints on the sample. The complete sets of data are inverted by the ptychography iterative engine (PIE): (1) A first guess of the object and the wavefront functions are estimated. (2) The corresponding diffracted wavefield is calculated for the first beam/sample position. (3) The wavefield magnitudes are set to the square root of the experimental intensities while the corresponding phases are kept unchanged. (4) The new wavefield is back-propagated to the sample plane. (5) A new object function is calculated from the new wavefield value, keeping constant the illumination function. The relationship between the new object estimate and the previous one ensures that a certain amount of the result obtained at the previous iteration is conserved. In addition, the updating of the object is not allowed in the whole object space but rather enforced in the region where the illumination intensity is large, at the considered beam/sample position. Steps 1 to 5 are then repeated for the successive beam/sample positions with the new object function as the starting object estimate. The complete cycle is repeated a few times before the roles of the illumination and object functions are exchanged in the iterative process: at Step 5, the object function is kept constant, while the illumination function is updated, with a formula similar to the one used for the object update case. The PIE runs, alternating updating of the object and illumination

function, until the convergence is reached, i.e. the scattered intensities correspond to the experimental ones and the beam/sample positions verify the overlapping conditions. Therefore, both illumination function and sample are retrieved at the same time, with the same resolution [35].

The method is highly interesting for measurements that are based on focused X-ray beams, where the illumination function is highly different from the unfocused planar illumination function. In the Bragg geometry, it should allow for a straightforwardly discrimination of the beam-curvature induced phase shift from the displacement-field induced phase shift case. While several demonstrations of the PIE approach have been reported in numerical [37,38] and experimental studies with X-rays [39,35] and visible light [40], no demonstration of its applicability in the Bragg geometry has been obtained so far. This is explained by the experimental difficulties encountered to apply the ptychographic approach to a nano-crystal in the Bragg condition. In addition to the experimental set-up used for Bragg CDI with a micro-focused beam, this new method necessitates a sample translation stage, with typical accuracy of the order of a few percent of the beam size (i.e. $5-10\,\mathrm{nm}$). In addition, the large acquisition time needed to acquire the full Bragg Ptychography data set requires a high beam-to-sample stability. Ideally, for a 3D nano-crystal such as the one presented here, the sample has to be placed in Bragg condition in the focal plane of the (sub-)microbeam. For each position of the sample with regard to the focal spot, the full 3D diffraction pattern has to be measured. Using a 2D area detector, the 3D diffraction pattern is obtained by scanning the incidence angle by a few tens of a degree along the rocking curve. Hence, modifications of the Bragg diffraction patterns observed for different regions of the illumination function can be attributed to the modifications of the local wavefront instead of the sample effective electron density. The reconstructions of both sample and illumination functions are performed with the PIE applied on the full 3D data set, without major modification.

6. Conclusion

We have demonstrated the possibility of applying Bragg CDI in 2D to image a nano-crystal of 100 nm size, using a micro-focused X-ray beam. We have shown that imaging the displacement field is more difficult and relies on the fine knowledge of the wavefront at the sample position. In the example shown here, the retrieved centro-symmetric phase field at the sample position could be described by wavefront curvature effects. The wavefront analysis problem is crucial for the development of Bragg CDI on weakly strained material. Therefore, the ptychography approach seems to be a good candidate to solve this question in the near future.

Acknowledgements

The authors gratefully acknowledge F. Bley and O. Thomas for their help during the experiment. A. Djazouli and the other staff members of ESRF are warmly acknowledged for their support. This work was partially supported by the French ANR (ANR-08-JCJC-0095-01).

References

[1] James, R.W. *The Optical Principles of the Diffraction of X-rays*; G. Bell and Sons: London, 1948.

[2] Guinier, A.; Dexter, D.L. *X-ray Studies of Material*; Interscience: New York, 1963.

[3] Stangl, J.; Holý, V.; Bauer, G. *Rev. Mod. Phys.* **2004,** *76,* 725–783.

[4] Lamberti, C. *Surf. Sci. Rep.* **2004,** *53,* 1–197.

[5] Renaud, G.; Lazzari, R.; Leroy, F. *Surf. Sci. Rep.* **2009,** *64,* 255–380.

[6] Sayre, D. *Acta Crystallogr.* **1952,** *5,* 843.

[7] Gerchberg, R.W.; Saxton, W.O. *Optik (Jena)* **1972,** *35,* 237–246.

[8] Fienup, J.R. *Appl. Opt.* **1982,** *21,* 2758–2769.

[9] Miao, J.; Charalambous, P.; Kirz, J.; Sayre, D. *Nature* **1999,** *400,* 342–344.

[10] Miao, J.; Ishikawa, T.; Johnson, B.; Anderson, E.H.; Lai, B.; Hodgson, K.O. *Phys. Rev. Lett.* **2002,** *89,* 088303.

[11] Robinson, I.K.; Vartanyants, I.A.; Williams, G.J.; Pfeifer, M.A.; Pitney, J. *Phys. Rev. Lett.* **2001,** *87,* 195505.

[12] Williams, G.J.; Pfeifer, M.A.; Vartanyants, I.A.; Robinson, I.K. *Phys. Rev. Lett.* **2003,** *90,* 175501.

[13] Takagi, S. *J. Phys. Soc. Jpn* **1969,** *26,* 1239–1253.

[14] Labat, S.; Chamard, V.; Thomas, O. *Thin Solid Films* **2007,** *515,* 5557–5562.

[15] Barty, A.; Marchesini, S.; Chapman, H.N.; Cui, C.; Howells, M.R.; Shapiro, D.A.; Minor, A.M.; Spence, J.C.H.; Weierstall, U.; Ilavsky, J.; Noy, A.; Hau-Riege, S.P.; Artyukhin, A.B.; Baumann, T.; Willey, T.; Stolken, J.; van Buuren, T.; Kinney, J.H. *Phys. Rev. Lett.* **2008,** *101,* 055501.

[16] Nishino, Y.; Takahashi, Y.; Imamoto, N.; Ishikawa, T.; Maeshima, K. *Phys. Rev. Lett.* **2009,** *102,* 018101.

[17] Shapiro, D.; Thibault, P.; Beetz, T.; Elser, V.; Howells, M.; Jacobsen, C.; Kirz, J.; Lima, E.; Miao, H.; Neiman, A.M.; Sayre, D. *PNAS* **2005,** *102,* 15343–15346.

[18] Pfeifer, M.A.; Williams, G.J.; Vartanyants, I.A.; Harder, R.; Robinson, I.K. *Nature* **2006,** *442,* 63–66.

[19] Diaz, A.; Mocuta, C.; Stangl, J.; Mandl, B.; David, C.; Vila-Comamala, J.; Chamard, V.; Metzger, T.H.; Bauer, G. *Phys. Rev. B* **2009,** *79,* 125324.

[20] Favre-Nicolin, V.; Eymery, J.; Koster, R.; Gentile, P. *Phys. Rev. B* **2009,** *79,* 195401.
[21] Minkevich, A.A.; Gailhanou, M.; Micha, J.S.; Charlet, B.; Chamard, V.; Thomas, O. *Phys. Rev. B* **2007,** *76,* 104106.
[22] Minkevich, A.A.; Baumbach, T.; Gailhanou, M.; Thomas, O. *Phys. Rev. B* **2008,** *78,* 174110.
[23] Diaz, A.; Chamard, V.; Mocuta, C.; Magalhães-Paniago, R.; Stangl, J.; Carbone, G.; Metzger, T.H.; Bauer, G. *New J. Phys.* **2010,** *12,* 035006.
[24] Chamard, V.; Diaz, A.; Stangl, J.; Labat, S. *J. Strain Anal.* **2009,** *44,* 533–542.
[25] Dollé, M.; Gosset, D.; Bogicevic, C.; Karolak, F.; Simeone, D.; Baldinozzi, G. *J. Eur. Ceram. Soc.* **2007,** *27,* 2061–2067.
[26] Diaz, A.; Mocuta, C.; Stangl, J.; Keplinger, M.; Weitkamp, T.; Pfeiffer, F.; David, C.; Metzger, T.H.; Bauer, G. *J. Synchrotr. Rad.* **2010,** *17,* 299–307.
[27] Robinson, I.K.; Pfeiffer, F.; Vartanyants, I.A.; Sun, Y.; Xia, Y. *Opt. Express* **2003,** *11,* 2329–2334.
[28] Schroer, C.G.; Boye, P.; Feldkamp, J.M.; Patommel, J.; Schropp, A.; Schwab, A.; Stephan, S.; Burghammer, M.; Schöder, S.; Riekel, C. *Phys. Rev. Lett.* **2008,** *101,* 090801.
[29] Takahashi, Y.; Nishino, Y.; Tsutsumi, R.; Kubo, H.; Furukawa, H.; Mimura, H.; Matsuyama, S.; Zettsu, N.; Matsubara, E.; Ishikawa, T.; Yamauchi, K. *Phys. Rev. B* **2009,** *80,* 054103.
[30] Livet, F. *Acta Cryst. A* **2007,** *63,* 87.
[31] Livet, F.; Bley, F.; Mainville, J.; Caudron, R.; Mochrie, S.G.J.; Geissler, E.; Dolino, G.; Abernathy, D.; Grübel, G.; Sutton, M. *Nucl. Instr. Meth. A* **2000,** *451,* 596–609.
[32] Vaxelaire, N.; Labat, S.; Chamard, V.; Thomas, O.; Jacques, V.; Picca, F.; Ravy, S.; Kirchlechner, C.; Keckes, J. *Nucl. Instr. Meth. B* **2010,** *268,* 388–393.
[33] Marchesini, S.; He, H.; Chapman, H.N.; Hau-Riege, S.P.; Noy, A.; Howells, M.R.; Weierstall, U.; Spence, J.C.H. *Phys. Rev. B* **2003,** *68,* 140101.
[34] Stadler, L.M.; Gutt, C.; Autenrieth, T.; Leupold, O.; Rehbein, S.; Chushkin, Y.; Grübel, G. *Phys. Rev. Lett.* **2008,** *100,* 245503.
[35] Thibault, P.; Dierolf, M.; Menzel, A.; Bunk, O.; David, C.; Pfeiffer, F. *Science* **2008,** *321,* 379–382.
[36] Quiney, H.M.; Peele, A.G.; Cai, Z.; Paterson, D.; Nugent, K.A. *Nature Phys.* **2006,** *2,* 101–104.
[37] Faulkner, H.M.L.; Rodenburg, J.M. *Phys. Rev. Lett.* **2004,** *93,* 023903.
[38] Rodenburg, J.M.; Faulkner, H.M.L. *Appl. Phys. Lett.* **2004,** *85,* 4795–4797.
[39] Rodenburg, J.M.; Hurst, A.C.; Cullis, A.G.; Dobson, B.R.; Pfeiffer, F.; Bunk, O.; David, C.; Jefimovs, K.; Johnson, I. *Phys. Rev. Lett.* **2007,** *98,* 034801.
[40] Thibault, P.; Dierolf, M.; Bunk, O.; Menzel, A.; Pfeiffer, F. *Ultramicroscopy* **2009,** *109,* 338–343.